JOURNAL OF COMPUTATIONAL PHYSICS 66, 255–273 (1986)

A New Method for Computing Normal Modes in Axisymmetric Toroidal Geometry Using a Scalar Form of Ideal MHD

F. WYSOCKI AND R. C. GRIMM[†]

Plasma Physics Laboratory, Princeton University,
Princeton, New Jersey 08544

Received October 16, 1984; revised January 22, 1985

DEDICATED TO THE MEMORY OF RAYMOND C. GRIMM

Analytic elimination of the two magnetic surface components of the displacement vector permits the normal ideal MHD equations to be reduced to a scalar form. A Galerkin procedure, similar to that used in the PEST codes, is implemented to determine the normal modes computationally. The method retains the efficient stability capabilities of the PEST 2 energy principle code, while allowing computation of the normal mode frequencies and eigenfunctions, if desired. The procedure is illustrated by comparison with earlier versions of PEST and by application to tilting modes in spheromaks, and to stable discrete Alfvén waves in tokamak geometry.

1. INTRODUCTION

Ideal MHD linear stability codes [1–3] have played an important role in helping to assess the stability properties of axisymmetric toroidal plasma configurations. As practical tools they are used on a daily basis at major tokamak laboratories to aid in the design of new experiments and in the analysis of experimental data. Since these applications frequently involve parameter surveys and, therefore, the running of many cases, a number of different versions of the codes exist. These take advantage of various optimizations that can be made when the interest is focused on specific stability issues. Additional improvements have occurred because the increased understanding of the nature of the instabilities, much of which has come from the computational studies, has led to various improvements in the numerical methods.

The necessity of carrying out some of these enhancements led to the development of PEST 2 [4], a code designed primarily to enable rapid computation of stability boundaries in parameter studies. This was achieved by the reduction of δW to a scalar form involving only one component of the displacement vector, $\boldsymbol{\xi}$, thereby

---

[†] Deceased August 1984.

0021-9991/86 $3.00

reducing the size of the matrix eigenvalue problem which has to be solved numerically to determine stability. In addition to the factor of 10–50 reduction obtained in typical execution times, improvements in the numerical representation of ξ greatly improved the convergence of the representation, so that for normal operation the time-consuming convergence studies can frequently be forgone [5].

While this procedure, which is basically a numerical treatment of the Energy Principle [6], is well suited for studying many stability issues, it has a major shortcoming in that it does not provide accurate estimates for the growth rates or eigenfunctions of the unstable normal modes. These can be valuable in attempting to make comparisons with experimental measurements and in assessing the need to include additional physics effects to the MHD model.

In the PEST 2 approach, the potential energy functional, $\delta W(\xi^*, \xi)$, was minimized subject to the constraint $\int d\tau \xi^* \cdot \boldsymbol{\rho} \cdot \xi = 1$, with tensor density, $\boldsymbol{\rho} \equiv \rho(\psi) \nabla\psi\nabla\psi/|\nabla\psi|^2$, rather than just the usual scalar, $\rho(\psi)$. Close to marginal stability, comparisons with the PEST 1 code showed that this procedure often gave approximations to the component $\xi \cdot \nabla\psi$ with many of the correct qualitative features of the true solution. However, the eigenvalue estimate, $\omega^2 \equiv$ extremum $\delta W(\xi^*, \xi)/\int d\tau(\xi^* \cdot \boldsymbol{\rho} \cdot \xi)$, has no relation (other than the sign) between the two norms.

Since many of the instabilities of interest have the property that $\xi \cdot \mathbf{B}$ and $\nabla \cdot \xi_\perp$ are very small, a "test function" approximation to ω^2 can be easily obtained from the PEST 2 calculation of $\xi \cdot \nabla\psi$. The approximation $\nabla \cdot \xi_\perp \approx 0$ is used to find the $\mathbf{B} \times \nabla\psi$ component of ξ, which is then added into an improved estimate of the kinetic energy form, $\int d\tau |\xi_\perp|^2$. Then $\omega^2 \approx \delta W(\xi_\psi^*, \xi_\psi)/\int d\tau \; \rho |\xi_\perp|^2$. An implementation of this technique showed that, for a variety of straightforward instabilities, growth rate estimates with errors of the order of 10–20% could be obtained. However, since the approximations are not good away from marginal stability or for small aspect ratio cases (where $\xi \cdot \mathbf{B}$ and $\nabla \cdot \xi_\perp$ are not necessarily small), such an approach has only limited value. Moreover, since the calculation of δW is done with considerably more accuracy, it is not at all aesthetically pleasing to have to rely on such an approximation.

The PEST 2 approach can, however, be straighforwardly generalized to obtain nonlinear eigenvalue formulation of the complete normal mode equations, which is of similar scalar form involving only the single component, $\xi \cdot \nabla\psi$, of the displacement vector. The surface components are eliminated analytically prior to the introduction of discretization, as opposed to previous methods which eliminate these components by utilizing sparse matrix techniques in solving $\mathbf{A} \cdot \mathbf{x} = \omega^2 \mathbf{B} \cdot \mathbf{x}$ after the full matrices are computed [22]. The generalization of PEST 2 is the subject of this report. We briefly describe the algebra involved and present the eigenvalue problem in the next section. In Section 3 a discussion of the numerical methods used to solve the equations is presented. Examples, illustrating the technique, are given in Section 4.

2. FORMULATION

The procedure we follow to reduce the normal mode equations to an eigenvalue problem involving only one dependent variable is analogous to that carried out in cylindrically symmetic systems, where the components ξ_θ, ξ_z are eliminated to give a second-order, differential equation for ξ_r[7]. The algebraic steps are, however, more complicated because of the coupling of different poloidal harmonics which occurs in toroidal geometry. The procedure depends on the fact that the two magnetic surface components of $\boldsymbol{\xi}$ can be eliminated surface-by-surface, involving only the inversion of surface operators, since in the appropriate coordinates no radial derivatives of these components occur in the original Euler equations. Because of this, it is essential to employ a flux coordinate system and to adopt an appropriate decomposition of $\boldsymbol{\xi}$ to obtain a form useful for numerical work.

The basic equations we begin with are the linearized normal mode equations of ideal MHD [6]

$$-\omega^2\rho\boldsymbol{\xi} = \mathbf{F}(\boldsymbol{\xi}), \tag{1}$$

where the displacement $\boldsymbol{\xi}(\mathbf{x}, t) = \boldsymbol{\xi}(\mathbf{x}) \exp(i\omega t)$,

$$\begin{aligned}\mathbf{F} \equiv {} & [\nabla\times(\mathbf{Q}+\xi_n\mathbf{J}\times\mathbf{n})]\times\mathbf{B} - \mathbf{n}[\mathbf{J}\times\mathbf{n}\cdot(\mathbf{Q}+\xi_n\mathbf{J}\times\mathbf{n})]\\ & + 2U|\nabla\psi|^2\,\mathbf{n}\xi_n + \nabla(\gamma p\nabla\cdot\boldsymbol{\xi}),\end{aligned} \tag{2}$$

$$\mathbf{Q} \equiv \nabla\times(\boldsymbol{\xi}\times\mathbf{B}), \qquad \mathbf{n} = \nabla\psi/|\nabla\psi|, \qquad \xi_n \equiv \boldsymbol{\xi}\cdot\mathbf{n}, \qquad \mathbf{J} = \nabla\times\mathbf{B} \tag{3}$$

and

$$2U = 2p'k_\psi + \sigma^2B^2/|\nabla\psi|^2 - \mathbf{B}\cdot\nabla[\sigma(\mathbf{s}\cdot\nabla\psi)/|\nabla\psi|^2] + \sigma q'/\mathscr{J}, \tag{4}$$

with $\sigma \equiv \mathbf{J}\cdot\mathbf{B}/B^2$ and $k_\psi = \mathbf{B}\times\mathbf{s}\cdot[\mathbf{B}/B\cdot\nabla(\mathbf{B}/B)]/B^2$. In Eqs. (2)–(4) we adopt the generalized PEST coordinate system [4] (ψ, θ, ζ) with Jacobian, $\mathscr{J} \equiv |\nabla\psi\times\nabla\theta\cdot\nabla\zeta|^{-1}$. Then

$$\mathbf{B} = \nabla\zeta\times\nabla\psi + q\nabla\psi\times\nabla\theta = \mathbf{s}\times\nabla\psi \tag{5}$$

with $\mathbf{s} \equiv \nabla\zeta - q\nabla\theta$. The safety factor, $q(\psi)$, is given by

$$q(\psi) = g(\psi)\langle\mathscr{J}/x^2\rangle, \tag{6}$$

where $g(\psi) = x^2\mathbf{B}\cdot\nabla\phi$, and $\langle\ \rangle$ denotes a surface average. The generalized toroidal angle ζ is related to the usual angle ϕ by $\zeta \equiv \phi - q\delta(\psi, \theta)$ and satisfies

$$\partial_\theta\,\delta(\psi, \theta) = (g\mathscr{J}/qx^2) - 1. \tag{7}$$

In Eq. (4), and throughout, a prime denotes differentiation with respect to ψ.

Following previous work, we write

$$\boldsymbol{\xi} = \xi^{\psi}\mathbf{B}\times\mathbf{s}/B^2 + i\xi^{s}\mathbf{B}\times\nabla\psi/B^2 + i\xi^{b}\mathbf{s}\times\nabla\psi/B^2, \tag{8}$$

so that the two surface components of Eq. (1) (obtained by taking the scalar products with $\mathbf{B}$ and $\mathbf{B}\times\nabla\psi$) can be written

$$-i\omega^2\rho\xi^b = \mathbf{B}\cdot\nabla(\gamma p\nabla\cdot\boldsymbol{\xi}) \tag{9}$$

and

$$\begin{aligned}-\omega^2\rho[i|\nabla\psi|^2\,\xi^s + (\mathbf{s}\cdot\nabla\psi)\,\xi^{\psi}] = {} & -B^2\nabla\psi\cdot[\nabla\times(\mathbf{Q}+\xi_n\mathbf{J}\times\mathbf{n})] \\ & + \mathbf{B}\times\nabla\psi\cdot\nabla(\gamma p\nabla\cdot\boldsymbol{\xi}).\end{aligned} \tag{10}$$

To take advantage of algebraic simplifications which occur in the detailed analysis, we introduce new variables,

$$\bar{\xi}^b \equiv (i\xi^b/\mathcal{J}B^2 + \nabla\psi\cdot\nabla\theta\xi^{\psi}/x^2B^2)\exp(inq\delta),$$

$$\bar{\xi}^s \equiv [\xi^s + i(q\delta)'\xi^{\psi}]\exp(inq\delta),$$

and

$$\bar{\xi}^{\psi} \equiv \xi^{\psi}\exp(inq\delta), \tag{11}$$

and solve Eqs. (9) and (10) to express $\bar{\xi}^b$, $\bar{\xi}^s$ in terms of $\bar{\xi}^{\psi}$.

The algebraic steps are straightforward, but tedious. In the following we present the results for the case of an axisymmetric toroidal equilibrium, which allows some simplification since we can write $\boldsymbol{\xi}(\mathbf{x}) = \boldsymbol{\xi}(\psi, \theta)\exp(-in\zeta)$ and consider each toroidal harmonic, n, separately. The procedure can obviously be generalized to any configuration with nested flux surfaces. We find that Eq. (9) can be written in the form,

$$\pi_0\bar{\xi}^b = \pi_1\bar{\xi}^s + \pi_2\bar{\xi}^{\psi} \tag{12}$$

where the operators π_i are

$$\pi_0 = -\rho\omega^2\mathcal{J}^2B^2/(\gamma p) + \pi, \tag{13}$$

$$\pi = ing\mathcal{J}_{\theta}/x^2 + n^2g^2\mathcal{J}^2/x^4 + inq\delta_{\theta\theta} + (2ing\mathcal{J}/x^2)\,\partial_{\theta} - \partial_{\theta}\mathcal{J}^{-1}\,\partial_{\theta}\mathcal{J}, \tag{14}$$

$$\pi_1 = in^2g\mathcal{J}/x^2 - n\partial_{\theta} - i\pi g/(\mathcal{J}B^2), \tag{15}$$

and

$$\pi_2 = -\rho\omega^2\mathcal{J}^2\nabla\psi\cdot\nabla\theta/(x^2\gamma p) - ing\mathcal{J}'/x^2 + \partial_{\theta}\mathcal{J}'/\mathcal{J} - (ing\mathcal{J}/x^2)\,\partial_{\psi} + \partial_{\theta}\partial_{\psi}. \tag{16}$$

Similarly, Eq. (10) yields

$$\Gamma_0\bar{\xi}^s = \Gamma_1\bar{\xi}^b + \Gamma_2\bar{\xi}^{\psi} \tag{17}$$

with

$$\begin{aligned} \Gamma_0 &= i|\nabla\psi|^2(\rho\omega^2/B^2 - n^2/x^2) + i\mathscr{J}^{-1}\,\partial_\theta x^2\mathscr{J}^{-1}\,\partial_\theta - i\gamma p n^2|\nabla\psi|^2/(x^2B^2) \\ &\quad - \gamma p n g/(\mathscr{J}B^2)\,\partial_\theta - i\Gamma_1 g/(\mathscr{J}B^2), \end{aligned} \tag{18}$$

$$\begin{aligned} \Gamma_1 &= -\gamma p[g\mathscr{J}^{-1}\,\partial_\theta\mathscr{J}^{-1}\,\partial_\theta\mathscr{J} - inq\delta_{\theta\theta}\,g/\mathscr{J} + (in(|\nabla\psi|^2 - g^2)/x^2)\,\partial_\theta \\ &\quad + in|\nabla\psi|^2\,\mathscr{J}_\theta/(x^2\mathscr{J}) + n^2 g\mathscr{J}|\nabla\psi|^2/x^4]/B^2, \end{aligned} \tag{19}$$

and

$$\begin{aligned} \Gamma_2 &= \rho\omega^2\mathscr{J}g\nabla\psi\cdot\nabla\theta/(x^2B^2) - in(x^2p' + gg')/x^2 - n^2g\mathscr{J}\nabla\psi\cdot\nabla\theta/x^4 \\ &\quad - in\gamma p\mathscr{J}'|\nabla\psi|^2/(\mathscr{J}x^2B^2) - (in|\nabla\psi|^2(1+\gamma p/B^2)/x^2)\,\partial_\psi \\ &\quad - (in\nabla\psi\cdot\nabla\theta/x^2)\,\partial_\theta - \gamma p g/(\mathscr{J}B^2)\,\partial_\theta\mathscr{J}'/\mathscr{J} - \gamma p g/(\mathscr{J}B^2)\,\partial_\theta\partial_\psi \\ &\quad - (gx^2/\mathscr{J}^2)\,\partial_\psi(\mathscr{J}/x^2)\,\partial_\theta + g\mathscr{J}^{-1}[\mathscr{J}(x^2/\mathscr{J})_\theta/x^2]'. \end{aligned} \tag{20}$$

In these expressions we have adopted the notation that subscripts with respect to θ represent θ-derivatives of equilibrium quantities; thus, for example, $\mathscr{J}_\theta \equiv \partial_\theta\mathscr{J}$. Also, all explicit ψ and θ derivatives act on whatever quantities appear to the right.

The formal solution of Eqs. (12) and (17) gives

$$\bar{\xi}^s = (\Gamma_0 - \Gamma_1\pi_0^{-1}\pi_1)^{-1}(\Gamma_1\pi_0^{-1}\pi_2 + \Gamma_2)\,\bar{\xi}_\psi \equiv \chi\bar{\xi}_\psi, \tag{21}$$

and

$$\bar{\xi}^b = \pi_0^{-1}(\pi_1\chi + \pi_2)\,\bar{\xi}_\psi \equiv \Phi\bar{\xi}_\psi. \tag{22}$$

Inspection of the explicit forms for these operators show that derivatives with respect to ψ occur only in π_2 and Γ_2, so that $\bar{\xi}^s$ and $\bar{\xi}^b$ can be formally eliminated by inverting operators which involve only derivatives in the magnetic surfaces.

To proceed further, we follow the variational formulation of the normal mode equations; i.e., we extremize the quadratic form [4]

$$\delta W = \int_p d\tau(|\mathbf{Q} + \xi^\psi\mathbf{J}\times\nabla\psi/|\nabla\psi|^2|^2 + \gamma p|\nabla\cdot\boldsymbol{\xi}|^2 - 2U|\xi^\psi|^2) + \int_v d\tau|\nabla\times A|^2, \tag{23}$$

where **A** is the vector potential for the perturbed vacuum magnetic field, subject to the norm $\int_p \rho|\boldsymbol{\xi}|^2\,d\tau = 1$. From Eqs. (8) and (11) we find

$$\begin{aligned} |\boldsymbol{\xi}|^2 &= \{[1 + g^2\mathscr{J}^2(\nabla\psi\cdot\nabla\theta)^2/x^4B^2]/|\nabla\psi|^2\}|\xi^\psi|^2 - ig\mathscr{J}\nabla\psi\cdot\nabla\theta(\bar{\xi}^{\psi *}\bar{\xi}^s - \bar{\xi}^\psi\bar{\xi}^{s *})/x^2B^2 \\ &\quad + |\nabla\psi|^2|\bar{\xi}^s|^2/B^2 + |\xi^b|^2/B^2, \end{aligned} \tag{24}$$

$$|\mathbf{Q} + \xi^\psi\mathbf{J}\times\nabla\psi/|\nabla\psi|^2|^2 = |A_1\xi^\psi|^2/|\nabla\psi|^2 + |A_2\xi^\psi|^2/B^2|\nabla\psi|^2 + |A_3\xi^\psi|^2/B^2 \tag{25}$$

with

$$A_1\xi^\psi = \mathscr{J}^{-1}(\partial_\theta - inq)\,\xi^\psi, \tag{26}$$

$$\begin{aligned} A_2\xi^\psi = \Bigg[&- g\frac{\nabla\psi\cdot\nabla\theta}{x^2}(\partial_\theta - inq) + \frac{g|\nabla\psi|^2(\mathscr{J}/x^2)'}{\mathscr{J}} \\ &+ \frac{i|\nabla\psi|^2\exp(-inq\delta)}{\mathscr{J}}\,\partial_\theta\chi\exp(inq\delta) \\ &+ \frac{n|\nabla\psi|^2 g}{x^2}\exp(-inq\delta)\,\chi\exp(inq\delta) \\ &- \frac{g(x^2p' + gg')}{x^2}\Bigg]\,\xi^\psi, \end{aligned} \tag{27}$$

$$\begin{aligned} A_3\xi^\psi = \Bigg\{ &\left[-g^2\frac{(\mathscr{J}/x^2)'}{\mathscr{J}} - in(q\delta)'\,B^2 + inq\frac{\nabla\psi\cdot\nabla\theta}{x^2} - \frac{(x^2p' + gg')}{x^2} \right] - B^2\,\partial_\psi \\ &- (\nabla\psi\cdot\nabla\theta/x^2)\,\partial_\theta - \frac{ig[\exp(-inq\delta)]}{\mathscr{J}}\,\partial_\theta\chi\exp(inq\delta) \\ &+ n\frac{|\nabla\psi|^2\exp(-inq\delta)}{x^2}\,\chi\exp(inq\delta)\Bigg\}\,\xi^\psi, \end{aligned} \tag{28}$$

and

$$\begin{aligned} \gamma p|\nabla\cdot\xi|^2 = \gamma p\,\Bigg| &\frac{\mathscr{J}'\bar{\xi}^\psi}{\mathscr{J}} + \partial_\psi\bar{\xi}^\psi + n\left(\frac{g^2}{x^2B^2} - 1\right)\bar{\xi}^s + \frac{ig}{\mathscr{J}}\,\partial_\theta(\bar{\xi}^s/B^2) \\ &- ing\mathscr{J}\,\frac{\bar{\xi}^b}{x^2} + \mathscr{J}^{-1}\,\partial_\theta(\mathscr{J}\bar{\xi}^b)\Bigg|^2 \equiv \gamma p|\Lambda\bar{\xi}^\psi|^2. \end{aligned} \tag{29}$$

Thus, since the perturbed vacuum potential energy contribution is given in terms of ξ^ψ on the plasma-vacuum interface (1), the quadratic forms can be written entirely in terms of ξ^ψ by using Eqs. (21) and (22) for $\bar{\xi}^s$ and $\bar{\xi}^b$. The final result can be expressed schematically as

$$\omega^2 K(\xi^{\psi *}, \xi^\psi \,|\, \omega^2) = \delta W(\xi^{\psi *}, \xi^\psi \,|\, \omega^2), \tag{30}$$

where K and δW are quadratic forms in ξ^ψ, each explicitly involving the eigenvalue ω^2. The eigenvalue problem, which is obtained after extremizing with respect to ξ^ψ, is therefore nonlinear in ω^2, and its numerical solution must be found by iteration.

3. NUMERICAL METHODS

3.1. *Overview*

The eigenvalue problem corresponding to Eq. (30) is solved by a straightforward generalization of the Galerkin method used in previous PEST codes [1, 4]. We begin by introducing the mixed finite-element Fourier expansion,

$$\xi^{\psi}(\psi, \theta, \zeta) = \sum_{l=-|L|}^{|L|} \sum_{m=1}^{M} \xi_{lmn} u_m(\psi) \exp[i(l\theta - n\zeta)], \tag{31}$$

into the quadratic forms associated with Eq. (30). The weak form of the normal mode equations can then be written as the generalized matrix eigenvalue problem,

$$W_{l'lm'm}(\omega^2)\, \xi_{lm} = \omega^2 K_{l'lm'm}(\omega^2)\, \xi_{lm}, \tag{32}$$

where the matrix elements of $\mathbf{W}(\omega^2)$ and $\mathbf{K}(\omega^2)$ are very complicated expressions obtained by following through the analysis of the last section. Each can be written in the form,

$$W_{l'lm'm}(\omega^2) = (2\pi)^2 \int d\psi [u_{m'} u'_{m'}] \begin{bmatrix} W_{l'l}(\omega^2) & Y^{+}_{l'l}(\omega^2) \\ Y_{l'l}(\omega^2) & Z_{l'l}(\omega^2) \end{bmatrix} \begin{bmatrix} u_m \\ u'_m \end{bmatrix}, \tag{33}$$

where the matrices $\mathbf{W}$, $\mathbf{Y}$, and $\mathbf{Z}$ are functions of ψ and depend in a known way on ω^2. These subsidiary matrices are evaluated surface-by-surface in the calculation, and involve the explicit inversion of the operators π_0 and $[\Gamma_0 - \Gamma_1 \pi_0^{-1} \pi_1]$ of Eqs. (21) and (22) in the Fourier space corresponding to the coordinate θ. The final result is too tedious to present in full detail here; instead we continue this section by briefly describing some of the most important steps in the calculation.

3.2. *Elimination of* ξ^s, ξ^b

The elimination of ξ^s and ξ^b proceeds by finding the Fourier matrix representation of the operators χ and Φ of Eqs. (21) and (22). We introduce the bracket notation,

$$\chi_{l'l} \equiv \langle l' | \chi | l \rangle = \frac{1}{2\pi} \oint d\theta \exp(-il'\theta)\, \chi \exp(il\theta), \tag{34}$$

so that

$$\chi_{l'l} = \langle l' | (\Gamma_0 - \Gamma_1 \pi_0^{-1} \pi_1)^{-1} (\Gamma_1 \pi_0^{-1} \pi_2 + \Gamma_2) | l \rangle \tag{35}$$

and

$$\Phi_{l'l} = \langle l' | \pi_0^{-1} (\pi_1 \chi + \pi_2) | l \rangle. \tag{36}$$

These expressions are evaluated in a straightforward manner and attention need only be given to two complications, viz., the treatment of the convolutions that occur in evaluating operator products and, second, the complications which occur because π_2 and Γ_2 explicitly involve ψ-derivatives.

To illustrate the convolution treatment we consider the evaluation of Eq. (35). This can be written formally as the infinite matrix product,

$$\chi_{l'l} = \langle l' | (\Gamma_0 - \Gamma_1 \pi_0^{-1} \pi_1)^{-1} | k \rangle \langle k | \Gamma_1 \pi_0^{-1} \pi_2 + \Gamma_2 | l \rangle, \tag{37}$$

TABLE I

Convergence of Convolution Truncation for the Equilibrium and Eigenmode Considered in Section 4.1

L^*	$\Omega^2 \equiv \omega^2[\rho q(s)^2 R^2/B_0^2]$
15	0.9246489
16	0.9246235
17	0.9246209
20	0.9246227
25	0.9246227

Note. The other parameters were; PEST-θ coordinates, $M=48$ and $L=15$. The growth rate is normalized to the poloidal Alfvén frequency at the plasma surface.

where $|k\rangle\langle k| = I$, the identity operator, and summation convention is assumed. Numerically, we truncate the infinite product, taking L^* terms, so that I is approximated by

$$I_{L^*} = \sum_{k=-|L^*|}^{|L^*|} |k\rangle\langle k|. \tag{38}$$

In the calculations we let L^* be an additional input parameter and, for fixed L, varied it until the results were satisfactorily converged. For every case we considered, taking $L \leqslant L^* \leqslant L+5$ was sufficient. This is illustrated in Table I where we present some convergence results for analytic equilibrium studies in Ref. [5]. With this prescription for evaluating matrix products, the remaining steps are straightforward; considering the first term of Eq. (37),

$$\begin{aligned}\langle l'|\,(\Gamma_0-\Gamma_1\pi_0^{-1}\pi_1)^{-1}\,|k\rangle &= \langle l'|\,\Gamma_0-\Gamma_1\pi_0^{-1}\pi_1\,|k\rangle^{-1}\\ &= (\langle l'|\Gamma_0|k\rangle - \langle l'|\Gamma_1|k'\rangle\langle k'|\pi_0|k''\rangle^{-1}\langle k''|\pi_1|k\rangle)^{-1}\end{aligned}$$

which can be evaluated from the expressions given in Eqs. (13), (14), (15), (18), and (19).

In the preceding discussion we have assumed that all the operators remain bounded, which they do, at least almost everywhere in the domain of ω^2. The exceptions are at the set of values of ω^2 which are eigenvalues of the operators π_0 and Γ_0. This set excludes all the eigenvalues of the normal modes (including the continuous spectra), except possibly marginally stable axisymmetric perturbations for which a proper treatment would have to follow the treatment in the Appendix of Ref. 4. For a given value of L, these $2(2L+1)$ values of ω^2 are the toroidal analogues of those which separate Sturmian from anti-Sturmian behavior of the spectrum of the cylindrical, diffuse linear pinch [8]. As in the cylindrical problem, it is our experience that the numerical solution, which involves iteration in ω^2, is for all practical purposes oblivious of these possible difficulties.

The second issue to comment on is the treatment of the ψ-derivatives in π_2 and Γ_2. These give rise to terms in **Y** and **Z** of Eq. (33), coming explicitly from the elimination of $\bar{\xi}^s$ and $\bar{\xi}^b$, as can be seen, for example, in the second term of Eq. (37). They are handled in a simple manner by splitting each of the operators as, for example,

$$\pi_2 = \bar{\pi}_2 + \tilde{\pi}_2\, \partial_\psi, \tag{39}$$

where $\bar{\pi}_2$ and $\tilde{\pi}_2$ do not involve ψ-derivatives. Then

$$\chi = \bar{\chi} + \tilde{\chi}\, \partial_\psi, \qquad \Phi = \bar{\Phi} + \tilde{\Phi}\, \partial_\psi \tag{40}$$

with

$$\bar{\Phi} = \pi_0^{-1}(\pi_1 \bar{\chi} + \bar{\pi}_2), \qquad \tilde{\Phi} = \pi_0^{-1}(\pi_1 \tilde{\chi} + \tilde{\pi}_2). \tag{41}$$

Thus, corresponding to the form Eq. (31) chosen for the representation of ξ^ψ, the two surface components can be expressed as

$$\xi^s(\psi, \theta, \zeta) = \sum_{l,m} (\bar{\xi}^s_{lm} u_m + \tilde{\xi}^s_{lm} u'_m) \exp[i(l\theta - n\zeta)], \tag{42}$$

where

$$\bar{\xi}^s_{lm} = \bar{\chi}_{ll'} \xi_{l'm}, \qquad \tilde{\xi}^s_{lm} = \tilde{\chi}_{ll'}, \xi_{l'm}, \tag{43}$$

with similar forms for ξ^b. The terms involving barred (twiddled) quantities eventually contribute to **W(Z)** matrix elements in Eq. (33).

As in previous work we have employed piecewise linear finite elements for the $u_m(\psi)$, which are the lowest order elements allowed for ξ^ψ, since it appears differentiated once with respect to ψ in Eq. (23). Lower order elements (the u'_m are Heaviside functions) are permitted for the two surface quantities, since no ψ-derivatives of these occur. It is interesting to note that, for finite M, Eq. (42) is distinctly different from previous methods [9, 10] in which Eq. (23) was varied with respect to each of the three components of $\boldsymbol{\xi}$, and in which only the terms corresponding to $\bar{\xi}^s_{lm}$ were included in the representation for ξ^s and ξ^b. Since, when ω^2 is an exact normal mode frequency, Eq. (42) is the discretization corresponding to Eq. (31), pollution of the spectrum [9] cannot be a serious problem in this constrained minimization. On the other hand, with respect to the convergence properties with the numerical parameter M, this method has no particular advantage over the previous schemes; both are $O(M^{-2})$ methods.

3.3. *Iteration in* ω^2

Since the matrix elements in Eq. (32) depend on ω^2, it is necessary to iterate to obtain the normal mode frequencies. To do this we use the simplest of schemes,

$$\mathbf{W}(\omega_p^2) \cdot \boldsymbol{\xi} = \omega_{p+1}^2 \mathbf{K}(\omega_p^2) \cdot \boldsymbol{\xi}, \qquad p = 0, 1, 2, \ldots, \tag{44}$$

and continue, until $|\omega_{p+1}^2 - \omega_p^2| \leqslant \varepsilon |\omega_p^2|$, with ε an appropriate small number. To

TABLE II

Convergence of the Eigenvalue Iteration for the Same Case as Table I

n	Ω_n^2
0	0.0
1	0.92462
2	0.76863
3	0.77502
4	0.77480
5	0.77480

commence the iteration, ω_0^2 must be chosen. Often, as for example when carrying out analysis of a sequence of slightly different equilibria, some prior knowledge of ω^2 will exist. If not, and the interest is in the issue of the stability of the equilibrium configuration, it is useful to take $\omega_0^2 = 0$. Then, this first step is essentially identical to the original PEST 2 formulation, the matrix elements representing δW must be the same, and the sign of ω_1^2 determines stability. Since the kinetic energy norm used here includes terms involving ξ^s and ξ^b, both of which are generally nonzero, the value of ω_1^2 will not be the same as that obtained from PEST 2. However, in the sense of Eq. (44), it is an approximation to the normal mode frequency. An example of the convergence properties of Eq. (44) is shown in Table II. It is seen that convergence can be quite rapid, typically requiring 2–3 steps to give 3–4 figures accuracy, which is about the maximum one should aim for with numerically determined equilibria.

This iteration is, of course, expensive computationally, since Eqs. (21) and (22) must be resolved at each stage. While many of the matrices involved can be saved from previous iteration steps, most of the computational time is involved in the surface-by-surface inversions for χ and Φ, and in the present coding of this method we have not gone to this effort. Consequently, the execution times scale comparably to the PEST 1 procedure. For practical applications, the present advantages lie in the fact that the PEST 2 formulation gives more accurate results for smaller values of M and L than with PEST 1. For example, for some internal kink mode calculations, the value of M for which instability is first detected can be typically 2–3 times smaller with this new procedure.

3.4. *Summary of the Numerical Steps*

The implementation of the steps described in the previous sections closely follows that of the PEST 2 code. We begin with a numerical equilibrium in flux coordinates, mapped onto an appropriate equally spaced ψ, θ mesh, typically with 97 surfaces and 128 θ-grid points. We select values of M, L, and L^* and remap the equilibrium to the new ψ mesh, which may be nonequally spaced, if desired. With piecewise linear elements the new ψ mesh has $2M+1$ grid points.

The calculation proceeds by computing the matrices **W**, **Y**, and **Z** of Eq. (33) on each ψ grid surface. This involves constructing the π and Γ matrices of Section 2, inverting the appropriate combinations to obtain χ and Φ, and then taking the appropriate Fourier transforms (using FFT routines) of the expressions in Eqs. (24)–(29). The **W** and **K** matrices of Eq. (32) are then obtained by carrying out the integrations over the radial finite elements by numerical quadrature (Simpson's rule). These matrices are block tridiagonal, consisting of $(M+1)$ blocks each of rank $(2L+1)$. The calculation of perturbed vacuum magnetic energy is identical to previous work [4] and lead to contributions to the elements $W_{l'lM'M}$. The eigenvalues, ω_{p+1}^2, of Eq. (44) are found by inverse iteration, using ω_p^2 as the accelerating parameter in the eigenvalue shift.

When the eigenvalue iteration is converged to the required accuracy, Eqs. (21) and (22) [or more precisely Eq. (43) and the equivalent form for $\bar{\xi}_b$] are used to construct the eigenvector $\boldsymbol{\xi}$. For this purpose, the matrices $\bar{\chi}$, $\tilde{\chi}$, $\bar{\Phi}$, and $\tilde{\bar{\Phi}}$ are saved in disk files when they are computed, during the calculation of the matrix elements.

Because of the modular structure of the PEST code, while the algebra associated with this procedure is more tedious than with PEST 2, the actual coding changes are quite modest. They amount essentially to the replacement of one subroutine of about 300 statements with new coding of about 1000 lines. Several additional arrays used as working storage to hold temporarily the π and Γ matrices slightly increased the memory requirements.

4. APPLICATION

In this section we give several examples to show the usefulness of these modifications to the PEST 2 code. First, we consider two cases which illustrate the convergence properties and allow a comparison with PEST 1. These are a simple external kink instability, which has been studied previously [5] when comparisons were made between various stability codes, and an internal kink mode, which provides a more difficult test because the growth rate is very small and the mode is highly localized. We then go on to compute a tilting mode in a spheromak configuration, because it was the desire to obtain growth rates for comparison with the Proto–S1 experiment which originally motivated this work. Finally, we find a stable, discrete shear Alfvén wave to illustrate that the techniques developed here are not restricted to instability studies.

4.1. *Tokamak External Kink Mode*

We consider the simple analytic equilibrium studied in Ref. [5], a small aspect ratio, elliptic cross-sectional configuration specified by

$$\Psi = \frac{1}{2ER^2q(0)}\left[x^2z^2 + \frac{E^2}{4}(x^2 - R^2)^2\right], \tag{45}$$

TABLE III

Convergence with Number of Finite Elements (M) and Fourier Modes (L) for the External Kink Mode of Section 4.1

L/M	24	36	48
a. PEST θ-coordinate $\Omega^2_\infty = 0.7755$			
10	0.7679	0.7693	0.7698
15	0.7730	0.7744	0.7748
20	0.7731	0.7744	0.7749
b. Equal arc θ-coordinate $\Omega^2_\infty = 0.7757$			
10	0.7723	0.7744	0.7750
15	0.7722	0.7742	0.7749
20	0.7722	0.7742	0.7749

Note. Ω^2_∞ is the extrapolated value.

with $R = 1$, $q(0) = 1.2$, $q(s) = 2.09$, $E = 2$, and $\varepsilon = \frac{1}{3}$. With no external conducting wall, so that the plasma torus is surrounded by an infinite vacuum region, the $n = 1$ external kink mode is unstable, and its growth rate [measured in units of the poloidal Alfvén time at the plasma surface, $\omega_a^2 = \rho q^2(s) R^2/B_0^2$] was computed previously by the PEST 1 and ERATO codes as 0.75 and 0.78, respectively [5]. Here we repeat the calculations using PEST and equal arc length θ-coordinates, and present the results in Table III. For each case we took $L^* = 51$ (see Table I), and set ε, the relative error between successive iterates in Eq. (44), to 10^{-6} (see Table II). Table III presents the results for a set of three different radial meshes (M) and three different sets of Fourier modes ($-L \leqslant l \leqslant L$). For both coordinate systems we see that the estimates are essentially converged out in l with $L = 15$; the equal arc system (Table IIIb) is extremely accurate even with $L = 10$, while the PEST coordinate system begins to display some departure at this point. Both systems have a $1/M^2$ variation with the number of finite elements, and extrapolation to infinity gives $\omega^2 = 0.7755$ and 0.7757 [for IIIa and IIIb, respectively], in good agreement with the previous estimates.

4.2. *Tokamak Internal Kink Mode*

The internal $l = 1$, $n = 1$ ideal MHD mode is usually unstable in tokamak configurations when a $q = 1$ surface lies in the plasma region and β is finite [11]. This mode has a small growth rate of typically several orders of magnitude smaller than the external kinks. Its eigenfunction is localized inside the $q = 1$ surface and decreases rapidly to zero outside. Because of the need to resolve this region accurately, studying such an instability provides a good test for a stability code. The mode is particularly difficult to determine near to the points of marginal stability, and in these regions grid packing near the $q = 1$ surface and the addition

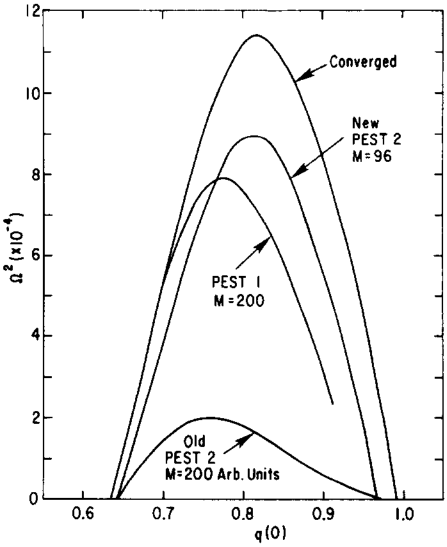

FIG. 1. Growth rate of the internal kink versus $q(0)$ calculated using PEST 1, original PEST 2, new PEST 2, and new PEST 2 converged to $M \to \infty$.

of specially tailored finite elements have been used to obtain very accurate results with PEST 2 [12]. The purpose here is not to address this aspect specifically, but to show that with this new version of PEST 2 it is possible to compute the growth rate and eigenfunction as well.

We consider an aspect ratio 3 toroidal equilibrium with circular plasma surface, computed from a flux coordinate equilibrium code, using the profiles $p(\psi) = p_0(1-\psi^{\alpha_1})$, $q(\psi) = q_0(1+\psi^{\alpha_2})$, with $\alpha_1 = 1.1$, and $\alpha_2 = 1.5$. The parameters p_0 and q_0 are such that $\beta_p \equiv 2\mu_0 \langle p \rangle / I_\phi^2 = 1.25$. A sequence of equilibria with constant β_p can be obtained by scaling the vacuum toroidal field to alter $q(0)$. We examine the stability of $n=1$ internal modes with $q(0)$ varying between 0.63 and 0.98, and present the results in Fig. 1. We give four sets of results; PEST 1 calculations with 200 radial elements, the new PEST 2 resuls with $M=200$ and no iterating on the eigenvalue (i.e., similar to the original PEST 2), and results after iterating with PEST 2, using 96 elements and after extrapolating to infinity. In all cases the mesh was uniformally spaced in the radial coordinate ψ, and the PEST θ angle was used with $-4 \leqslant l \leqslant 13$. In the PEST 2 calculations $L^* = 16$. The poloidal projection of the displacement vector ξ for $q(0) = 0.9$ computed from the new PEST 2 code is shown in Fig. 2.

Several comments can be made from the results shown in Fig. 1. First it is clear that with respect to determining the instability, both PEST 2 codes are considerably more accurate than PEST 1, which is expensive to run computationally ($\sim$5 min CRAY I time) with 200 elements. This is especially true when the $q=1$ surface lies close to the magnetic axis ($q(0) \approx 1$), because the equally spaced ψ mesh in PEST 1

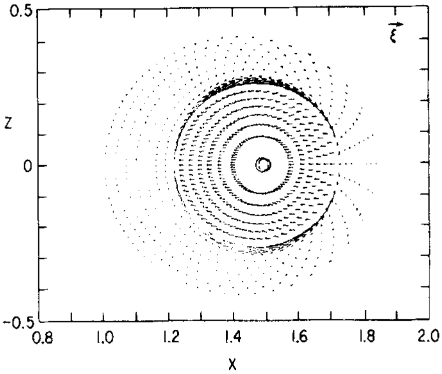

FIG. 2. Poloidal projection of the displacement vector, ξ, for the internal kink with $q(0)=0.9$, computed using the new PEST 2.

tends to weight regions near the plasma surface more heavily than near the axis. However, it can be seen that PEST 1 gives reasonable results when the $q=1$ surface lies further out towards the plasma surface. Even with 200 elements the PEST 1 code has difficulty finding instability, except where the growth rate is relatively large. With $M \leqslant 200$ it is also difficult to carry out a reliable extrapolation to the limit procedure, since the region where the errors scale as $1/M^2$ has not been reached. PEST 2 does not suffer these problems, except very close to the marginal points. By comparing the results near to the marginal point for the extrapolated curve and the results obtained by running in the original PEST 2 mode, we see that these can be accurately evaluated with $M=200$. With $M=200$ the new code follows the converged curve over most of the range with an error $\leqslant 5\%$ of the maximum growth rate. Thus, except near the marginal points, convergence studies are not really essential for many applications.

4.3. *Spheromak Tilting Mode*

The tilting mode was predicted analytically for force-free spherical and near-spherical spheromaks [13] and is observed experimentally [14]. Its presence is generally found to be highly destructive; therefore, a thorough understanding of the mode is required. The PEST 1 code has difficulty with small aspect ratio ($\varepsilon \to 1$) spheromak geometry which is alleviated in PEST 2 by switching from PEST θ coordinates to equal arc θ coordinates and using a different represetation of ξ. PEST 2 has been used to examine the stable points of the tilting and shifting modes for different shapes with and without nearby conducting walls [15]. However PEST 2's lack of physically meaningful growth rates have made comparison with experimental results difficult. The new formulation presented here allows accurate determination of these growth rates.

For this particular example we have numerically generated equilibrium with a shape described by

$$x = x_0 + a\cos(\theta + d\cdot\sin\theta),$$
$$z = \varepsilon a \sin(\theta)$$

with $x_0 = 2.75$, $a = 1.55$, $\varepsilon = 2.0$, $d = 0.35$.

The surface quantities $g(\psi)$ and $p(\psi)$ are chosen to be

$$g(\psi) = g_s + \Delta g \cdot Y,$$
$$p(\psi) = P_0 Y^2,$$

where

$$Y = \frac{\psi_{\text{edge}} - \psi}{\psi_{\text{edge}} - \psi_{\text{axis}}} \quad \text{and} \quad g_s/\Delta g = 10^{-3}.$$

The resulting safety factor q is 0.582 at the magnetic axis and 0.00419 at the edge, and the volume-averaged beta is 2.25%.

With no external conducting wall the fully converged growth rate is $\gamma^2 = 0.50\,\omega_A^2$, where the Alfvén transit frequency is defined as

$$\omega_A = B_0/R_0\sqrt{\rho_0}$$

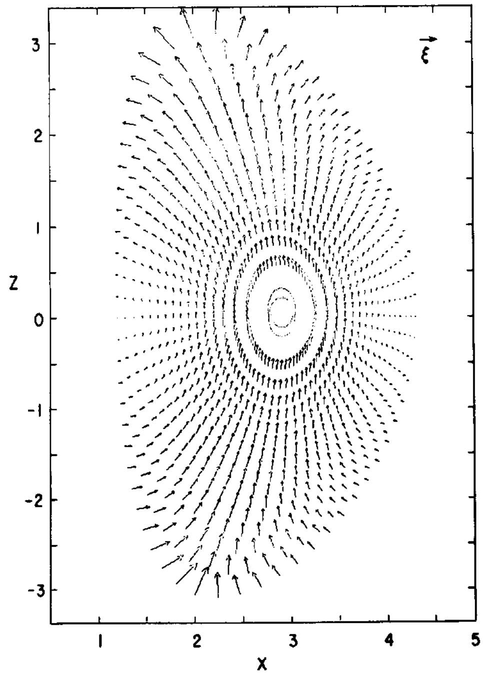

FIG. 3. Poloidal projection of the displacement vector, ξ, for the spheromak tilting mode computed using the new PEST 2.

and R_0 = major radius, B_0 = toroidal field at the magnetic axis, and the density, ρ_0, is assumed spatially constant.

The poloidal projection of the displacement vector ξ is shown in Fig. 3. These results are in good agreement with results from the ERATO stability code [16].

4.4. *Stable Shear Alfvén Wave*

In addition to the calculation of unstable perturbations, there is interest in modes in the stable part of the MHD spectrum. This is because the ability to compute the eigenfunctions can aid in our understanding of the instability driving mechanisms, and also because these stable oscillations are of interest for wave heating schemes. In the stable part of the spectrum there are both discrete modes and continuous bands of eigenfunctions associated with the shear Alfvén branch. The global shear Alfvén modes occur in cylindrical configurations [17, 18] and in a torus [18, 19], where additional discrete modes arise in the gaps between the continuum bands because of toroidal coupling of modes with different poloidal harmonics.

Because of the large number of stable eigenvalues associated with any reasonably accurate numerical representation of linearized ideal MHD equations, computation of the global Alfvén waves is complicated. One approach, which has been tried with PEST 1, entails calculation of all the eigenvalues of the discretized linear normal mode equations, using a wide resolution. By examining the radial structure of the eigenfunctions, it is possible to identity the discrete modes of interest. This gives an approximate eigenvalue estimate which can be used in an iterative eigenvalue scheme with more spatial resolution. Alternatively, an eigenvalue estimate can be obtained from a WKB local (ballooning mode) analysis of the problem, which

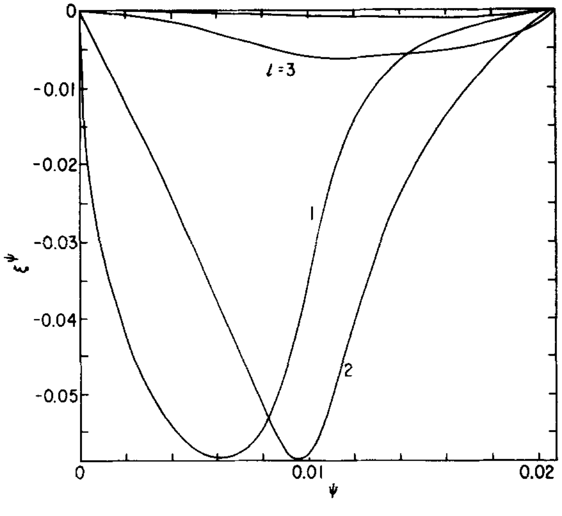

FIG. 4. Radial structure of the Fourier harmonics of ξ^ψ for a global Alfvén mode.

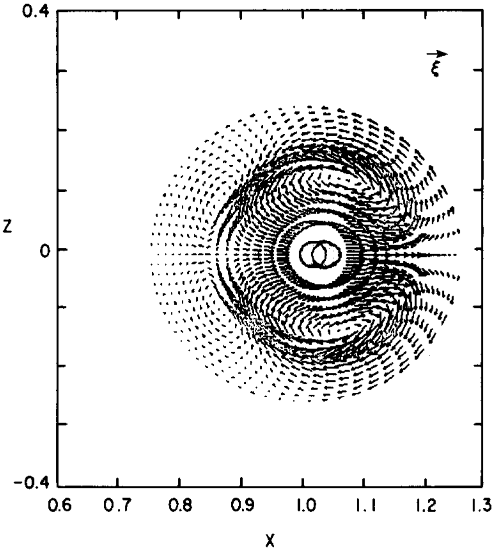

FIG. 5. Poloidal projection of the displacement vector, ξ, for the same global Alfvén mode of Fig. 4.

determines the gaps between the shear Alfvén wave continua surface by surface [20]. We consider an $n=1$ internal mode in an aspect ratio 4 toroidal equilibrium, with $\beta \sim 2\%$ and $1.05 < q < 2.3$. Using the approximation given from the localized analysis, we used the method of this paper to compute the global mode. The calculations were carried out with $M=48$ and $-8 < l < 12$. The radial structure of various Fourier harmonics is displayed in Fig. 4, and the poloidal projection of ξ is given in Fig. 5. The mode is seen to consist primarily of $l=1$ and 2 components,

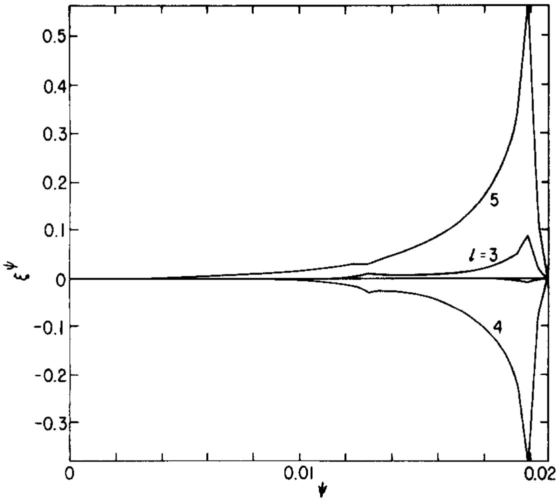

FIG. 6. Radial structure of the Fourier harmonics of ξ^{ψ} for a mode in the Alfvén continuum.

with a small coupling to $l = 3$ towards the plasma surface. In terms of the numerical calculation, the procedure behaves similarly to when it is used to compute unstable modes with respect to the number of iterations required, and no difficulties associated with inverting the operators in Eqs. (21) and (22) were observed. We also computed modes in the continuum, an example is given in Fig. 6.

5. DISCUSSION

In this paper we have described a numerical procedure which extends the efficient techniques of the PEST 2 stability code to enable an accurate estimate of the growth rates and eigenfunctions associated with the normal modes. The formulation followed that of PEST 2 in the reduction of δW to a quadratic form involving only one component of the displacement vector, but, by employing the correct kinetic energy normalization, the resulting eigenvalue problem was nonlinear. Utilizing identical numerical procedures, the normal mode frequencies and eigenfunctions were obtained by a straightforward iteration.

The numerical method was applied to several typical problems to illustrate the convergence properties and to make comparison with previous results. When implemented on a modern large scale computer (such as the CRAY 1), these results show that sufficient resolution can be obtained and that careful convergence studies, which were essential with the first generation of stability codes, can now frequently be avoided. It was also shown that the method can be applied to determine modes in the stable part of the MHD spectrum.

For axisymmetric toroidal equilibria, the full range of features available with the extended PEST 2 formulation should provide for an accurate ideal MHD analysis of most interesting confinement systems with $n \lesssim 10$–20. The improved efficiency of this scalar formulation will probably allow for an analogous examination of fully three-dimensional configurations, such as stellarators, where constraints imposed during the accurate calculation of MHD equilibria have the stability to low-n modes unresolved [21]. Finally, since the method does not rely implicity on the variational properties of the ideal MHD equations, the successful iteration for the eigenvalues demonstrated here suggests that similar techniques may be usefully applied to other toroidal systems, where the normal mode equations are not Hermitean. This situation occurs when additional physics (such as equilibrium flows and various dissipative processes) is included to improve the ideal MHD description of the confined plasma.

ACKNOWLEDGMENTS

The authors are grateful for many useful discussions with Dr. J. Manickam. He kindly provided the equilibrium and PEST 1 results for Fig. 5. We also wish to thank Dr. M. S. Chance and Dr. F. Cheng who provided the incentive and the data for the calculation of Section 4.4. We gratefully acknowledge the computational assistance of Mr. A. E. Miller.

This work supported by U.S. Department of Energy Contract DE-AC02-76-CHO-3073.

REFERENCES

1. R. C. GRIMM, J. M. GREENE, AND J. L. JOHNSON, *Methods Comput. Phys.* **16**, 253 (1976).
2. R. GRUBER, F. TROYON, D. BERGER, L. C. BERNARD, S. ROUSSET, R. SCHREIBER, W. KERNER, W. SCHNEIDER, AND K. V. ROBERTS, *Comput. Phys. Comm.* **21**, 323 (1981).
3. L. C. BERNARD, F. J. HELTON, AND R. W. MOORE, *Comput. Phys. Comm.* **24**, 377 (1981).
4. R. C. GRIMM, R. L. DEWAR, AND J. MANICKAM, *J. Comput. Phys.* **49**, 94 (1983).
5. M. S. CHANCE, J. M. GREENE, R. C. GRIMM, J. L. JOHNSON, J. MANICKAM, W. KERNER, D. BERGER, L. C. BERNARD, R. GRUBER, AND F. TROYON, *J. Comput. Phys.* **28**, 1 (1978).
6. I. B. BERNSTEIN, E. A. FRIEMAN, M. D. KRUSKAL, AND R. M. KULSRUD, *Proc. Roy. Soc. London Ser. A* **244**, 17 (1958).
7. K. HAIN, R. LÜST, AND A. SCHLÜTER, *Z. Naturforsch. A* **12**, 833 (1957).
8. J. P. GOEDBLOED AND P. H. SAKANAKA, *Phys. Fluids* **17**, 908 (1974).
9. K. APPERT, D. BERGER, R. GRUBER, AND J. RAPPAZ, *J. Comput. Phys.* **18**, 284 (1975).
10. D. BERGER, R. GRUBER, AND F. TROYON, *Comput. Phys. Comm.* **11**, 313 (1976).
11. W. KERNER, R. GRUBER, AND F. TROYON, *Phys. Rev. Lett.* **44**, 536 (1980).
12. J. MANICKAM, R. C. GRIMM, AND R. L. DEWAR, *Comput. Phys. Comm.* **24**, 355 (1981).
13. M. N. ROSENBLUTH AND M. N. BUSSAC, *Nucl. Fusion* **19**, 489 (1979).
14. C. MUNSON, A. JANOS, F. WYSOCKI, AND M. YAMADA, Princeton Plasma Physics Laboratory Report, PPPL-2019, 1983 (unpublished).
15. S. C. JARDIN, M. S. CHANCE, R. L. DEWAR, R. C. GRIMM, AND D. A. MONTICELLO, *Nucl. Fusion* **21**, 1203 (1981).
16. CH. PFERSICH, R. GRUBER, AND F. TROYON, *Nucl. Fusion* **23**, 1127 (1983).
17. M. S. CHANCE, J. M. GREENE, R. C. GRIMM, AND J. L. JOHNSON, *Nucl. Fusion* **17**, 65 (1977).
18. K. APPERT, R. GRUBER, AND J. VACLAVIK, *Phys. Fluids* **17**, 1471 (1974).
19. S. M. MAHAJAN, D. W. ROSS, AND G. L. CHEN, *Phys. Fluids* **26**, 2195 (1983).
20. C. Z. CHENG, L. CHEN, AND M. S. CHANCE, Princeton Plasma Physics Laboratory Report PPPL-1643, 1980 (unpublished).
21. F. BAUER, O. BETANCOURT, AND P. GARABEDIAN, *J. Comput. Phys.* **35**, 341 (1980).
22. D. S. SCOTT AND R. GRUBER, *Comput. Phys. Comm.* **23**, 115 (1981).